Journal of Materials Chemistry A

Accepted Manuscript

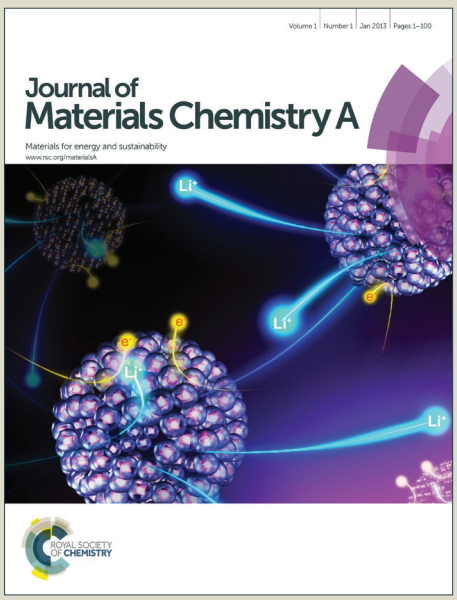

ROYAL SOCIETY OF CHEMISTRY

www.rsc.org/materialsA

Journal Name Journal of Materials Chemistry A Dynamic Article Links ►

Cite this: DOI: 10.1039/c0xx00000x

www.rsc.org/xxxxxx

ARTICLE TYPE

Design of graphene-coated hollow mesoporous carbon spheres as high performance electrodes for capacitive deionization

Hui Wang, Liyi Shi, Tingting Yan, Jianping Zhang, Qingdong Zhong and Dengsong Zhang*

Received (in XXX, XXX) Xth XXXXXXXXX 20XX, Accepted Xth XXXXXXXXX 20XX

DOI: 10.1039/b000000x

Graphene-coated hollow mesoporous carbon spheres (GHMCS) are rationally designed and originally used as the efficient electrode material for capacitive deionization. The GHMCS is fabricated by a simple template-directed method using the phenolic polymer coated polystyrene spheres as templates. The resulted graphene-based composites have a hierarchically porous nanostructure with hollow mesoporous carbon spheres uniformly embedded in the graphene sheets. The hierarchically porous structure of GHMCS electrode can guarantee fast transport of salty ions, and the improved special surface area of GHMCS provides more adsorption sites for the formation of electric double layer. In addition, the graphene sheets in the GHMCS as the interconnected conductive networks lead to faster charge transfer. The unique GHMCS structure exhibits enhanced electrochemical performance with a higher specific capacitance, lower inner resistance and long cycling lifetime. Besides, a remarkable capacitive deionization behavior of GHMCS with low energy consumption is obtained in a NaCl solution. The proposed carbon composites architectures are expected to lay the foundation for the design and fabrication of high-performance electrodes in the field of energy and electrochemistry.

1. Introduction

Water scarcity is one of the most serious challenges worldwide, and it will become worse with the population growth, the industrial development, and the contamination of available freshwater resources. The desalination of seawater and brackish water is a good way to solve this issue.[1] Traditional desalination processes including the reverse osmosis and thermal separations are commonly applied with such shortcomings as high cost, excessive energy consumption, or less environment-friendly.[2] Emerging as a novel desalination technology, capacitive deionization (CDI) has attracted more and more attention recently. The CDI is an electrochemical process based on the electric double-layered capacitors. When the external voltage is applied, salty ions in the solution move to the electrode with opposite charge and form an electric double layer (EDL). Once the charge is removed, the salty ions will desorb and return to the bulk solution.[3-5] Hence, as a low-pressure and non-membrane desalination process, the CDI is considered to be an energy-efficient, environment-friendly and low-cost alternative for desalination with no secondary waste.[6, 7]

On basis of the above mechanism, the surface properties of electrode materials are crucial to the CDI capacity. Carbon materials such as activated carbon,[8] carbon aerogels,[6] and mesoporous carbon[9] are commonly used candidates for CDI electrodes due to their large surface area and reasonable porous structure. Activated carbon and carbon aerogels were most used as the electrode for water desalination, but the CDI capacity was unsatisfactory due to the large amount of micropores restricting the ion diffusion and accessibility. Mesoporous carbon has narrow pore distribution and enormous mesoporous channels, which is favorable to the transportation and penetration of salty ions. Hence, mesoporous carbon displays a better CDI performance than conventional activated carbon as reported previously.[4] However, the limitation such as low effective surface area restricts the improvement the electrosorption capacity of mesoporous carbon electrode.[10] Therefore, significant efforts have been focused on the preparations of novel electrode materials with a reasonable porous structure currently. It is generally acknowledged that a hierarchically porous carbon combines the structural advantages of macropores and micro/mesopores. For the hierarchically porous carbon, macropores serving as an ion-buffering reservoir guarantee a shorter ion diffusion distance to the pores, and micro/mesopores can provide fast pathways and large accessible surface area for the ion transport and charge storage.[11] With regard to the superior pore structure, the hierarchically porous carbon has been demonstrated to be a potential electrode material for electrochemical capacitors and lithium-ion batteries.[12-14] Unfortunately, such inevitable drawbacks of hierarchically porous carbon as low conductivity and high energy cost still restrict the CDI application.

As well known, electrode materials with high conductivity is beneficial to the ion transport into the bulk of electrode as well as the effective charge holding.[15-17] Graphene, a two-dimensional carbon material with such fascinating properties as excellent conductivity, large theoretical special surface area, good chemical inertia and remarkable mechanical flexibility, has been widely

Cite this: DOI: 10.1039/c0xx00000x

www.rsc.org/xxxxxx

ARTICLE TYPE

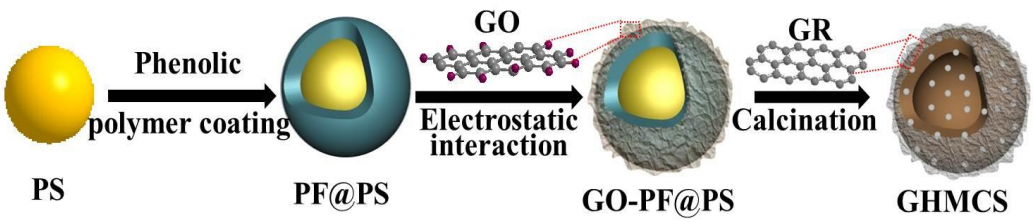

Scheme 1 Schematic illustration of graphene coated hollow mesoporous carbon spheres(GHMCS).

used in energy storage and electrosorption fields.[18-20] Most recently, the graphene as electrodes for the CDI have been investigated by us and other groups.[21-23] Li et al found that graphene-like nanoflakes exhibited a quite better CDI performance than the commercial activated carbon due to the higher conductivity.[23] In our former reports, we proved that the graphene obtained by a novel pyridine-thermal strategy showed an enhanced electrosorption performance than that reduced by hydrazine.[21] However, the electrosorption capacity of graphene is still far away from the anticipated value. The irreversible aggregation and restacking of graphene sheets commonly exists owing to the strong π-π interactions and van der Waals force between the planer basal planes of graphene sheets.[24, 25] The easy aggregation of graphene during the processing largely reduces its surface area and lessens the number of electrochemically active sites, resulting in a much lower electrosorption capacity for CDI electrodes. Thus, it is urgent to seek proper ways to solve the aggregation of graphene. Until now, the most used route to solve this issue is adding "spacers" between the graphene sheets. Various "spacers" such as metal oxides, conductive polymers, and carbon materials were chosen to incorporate into the interlayers of graphene.[26-28] However, most of the non-carbon "spacers" improve the electrochemical properties by increasing the pseudo-capacitance, which is not helpful to the improvement of CDI capacity. Besides, the carbon "spacers" such as activated carbon and mesoporous carbon are usually clumpy and massive, which cannot be well distributed in the graphene sheets and thus it is hard to ensure the effective exfoliation of graphene sheets within the whole composite structure. Therefore, it is desirable to solve the inhomogeneous distribution of "spacers" in graphene-based materials, and further improve the exfoliation of graphene.

As discussed above, the hierarchically porous carbon and graphene have the distinct advantage and the corresponding disadvantage when used individually. Therefore, a novel template-directed assembly for graphene coated hollow mesoporous carbon spheres (GHMCS) with a hierarchical pore structure are rationally designed and originally used as the electrode material for the CDI. Specifically, the phenolic polymer coated polystyrene spheres (PF@PS) prepared through a hydrothermal reaction were designed as the templates for the fabrication of GHMCS architecture. The brief formation process is shown in **Scheme 1**. Firstly, the PF@PS templates were well prepared, and then templates and the graphene oxide (GO) were mixed homogeneously due to the electrostatic interactions. Afterwards, the subsequent vacuum filtration was conducted to realize the GO-coated structure. The resulted composites (GO-PF@PS) were dried and calcinated to remove PS spheres and to thermally reduce GO to graphene. The resulted graphene-coated architectures were the GHMCS. The GHMCS took full advantages of the hierarchically mesoporous carbon spheres (HMCS) and graphene. The good distribution of HMCS embedded in the graphene sheets due to the electrostatic self-assembly prevented the aggregation and restacking of graphene.

Most importantly, the GHMCS had a unique hierarchical pore structures resulting from the HMCS and the graphene wrappings. Hence, the GHMCS could provide a superior pore structure for the enhancing ion infiltration, and the electrosorption capacity was greatly improved during the CDI process. Besides, this hierarchical structure exhibited great conductivity due to the existence of graphene sheets, which could guarantee fast charge transfer and lower energy consumption in the CDI application.

2. Experimental Section

2.1 Preparation

All the chemicals were purchased from Sinopharm Chemical Reagent Company and used without further purification except styrene. Before preparation, styrene monomer was washed with NaOH aqueous solution (0.1 M) and distilled water four times in a separatory funnel, and then purified by the reduced pressure distillation.

Typical synthesis of PF@PS nanospheres: The PS spheres with the diameter of 180 nm were prepared according to the previous report.[29] Firstly, the PS spheres (150 mg) were dispersed in deionized water (50 mL), then an aqueous solution (20 mL) of phenol (0.188 g) and an aqueous solution (10 mL) of hexamethylenetetramine (0.14 g) were added. After stirring gently for about 15 min, the solution was transferred into a 100 mL Teflon-lined autoclave and heated at 160 ^{o}C for 4 h. The PS@PF spheres were collected by centrifugation and washed several times with deionized water and pure ethanol. The as-prepared PF@PS nanospheres were re-dispersed in deionized water to obtain an aqueous suspension (3 wt.%) for the further application.

Synthesis of GO-PF@PS nanospheres: To assemble graphene-

based hierarchical architectures, GO was prepared initially by the Hummers' method. Typically, the dried GO powder was dispersed into deionized water with a concentration of 3 mg mL^{-1} by continuous ultrasonication. The typical procedure to prepare GO-PF@PS composite as follows: 20 mL of GO dispersion was dropped into the aqueous suspension PF@PS with the mass of 6 g under magnetic stirring, and the homogeneous colloidal suspension of PF@PS and GO hydrosol was obtained through ultrasonication about 1-2 h. After that, assembly of PF@PS spheres and GO sheets were realized through the vacuum filtration on a millipore filter. The above composites (GO-PF@PS) were peeled off from the filter and air dried at 40 ^{o}C overnight. The GO-PF@PS composites were annealed at 150 ^{o}C for 1 h and 900 ^{o}C for 2 h under N_2 atmosphere with a heating rate of 1 ^{o}C min^{-1} in a tubular furnace. GO within the composite film was thermally reduced into graphene and the PF was carbonized, while PS microspheres were removed and the HMCS were formed simultaneously, so as to get the GHMCS. The sample was prepared by a similar procedure but with no PF@PS templates or GO introduced for comparison, so as to resulting in a compact graphene (GR) and HCS.

2.2 Characterization

The morphologies were also examined by field emission scanning electron microscopy (SEM, JEOL JSM-700F). The morphologies were observed by transmission electron microscopy (TEM, JEOL JEM-200CX), and powdered samples were dispersed in ethanol by ultrasonication for 10 min in an ultrasonic bath. X-Ray diffraction (XRD) measurements were taken on a Rigaku D/MAX-RB X-ray diffractometer using Cu Kα radiation (40kV, 20 mA) and a secondary beam graphite monochromator. The Raman spectra were recorded on a spectrometer (JY H800UV) equipped with an optical microscope at room temperature. For excitation, the 514.5 nm line rom an Ar+ ion laser (Spectra Physics) was focused, with an analyzing spot of about 1 mm, on the sample under the microscope. Nitrogen sorption isotherms were measured with an ASAP 2020 (Micromeritics) at 77 K. Before the measurements, all samples were degassed overnight at 493 K in a vacuum line. The Brunauer–Emmett–Teller (BET) method was utilized to calculate the specific surface areas and the pore volumes, and the pore size distributions were derived from the desorption branches of the isotherms using the Barrett–Joyner–Halenda (BJH) model. The X-ray photoelectron spectroscopy (XPS) was recorded on a Perkin-Elmer PHI 5000C ESCA system equipped with a dual X-ray source, using the MgKα (1253.6 eV) anode and a hemispherical energy analyser. The back ground pressure during data acquisition was kept below 10−6 Pa. All binding energies were calibrated using contaminant carbon (C 1s = 284.6 eV) as a reference. Thermal decomposition of the solid was studied by thermogravimetry and differential thermal analysis (TG) using an SDT Q600 TA instrument at a heating rate of 10 ^{o}C/min from room temperature to 1000 ^{o}C. The electrochemical performance of the electrodes was evaluated by cyclic voltammetry (CV), the electrochemical impedance spectroscope (EIS) using a CHI 660D. Galvanostatic charge–discharge (GC) and energy consumption measurments were conducted on an automatic LAND battery test instrument. All the electrochemical properties were measured from a 3-electrode system in a NaCl solution.[3]

2.3 Batch mode CDI experiments

The CDI electrodes were fabricated by mixing 80 wt. % of the active component, 10 wt. % of acetylene black and 10 wt. % of polytetrafluoroethylene (5 wt. % aqueous solutions) homogenously, and then the ethanol was added into the mixture and then the slurry was pressed onto graphite sheets and dried at above 110 ^{o}C overnight. The size of electrode is 50 mm × 60 mm × 0.3 mm. The CDI performance of electrodes was measured in a batch mode electrosorptive experiment, which was conducted in a continuous recycling system as shown in our previous publication.[30] The CDI system herein included two sided electrodes separated by an insulated spacer. The NaCl aqueous solution with an initial conductivity of 68.0 μs cm^{-1} in a total volume of 60 mL was supplied to the cell using a pump with a flow rate of 25 mL min^{-1}. The electrode mass is 0.5 g. The concentration change of the solution was measured by connecting a conductivity meter at the outlet of the cell, where the solution was released.

3. Results and discussion

3.1. Characteristics

SEM and TEM were conducted to reveal the detailed morphology and structure of GHMCS, and the images are shown in Fig. 1. In order to prepare GHMCS, the PF@PS was firstly synthesized as the templates by a hydrothermal reaction. As shown in Fig. 1A-B, the PF@PS keeps spherical structure and the average diameter

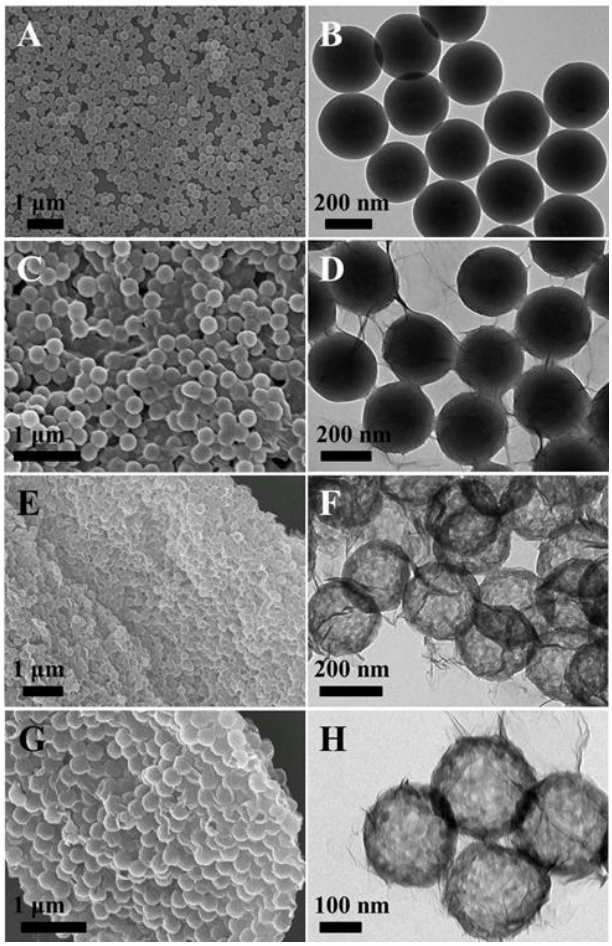

Fig.1 SEM and TEM images of (A-B) PF@PS; (C-D) GO-PF@PS and (E-H) GHMCS.

is about 290 nm, suggesting the PF is well coated on the surface of PS spheres (180 nm, Fig. S1). Based on the TEM observation, the thickness of coated PF layer is estimated to be approximately 55 nm. As seen from the SEM image of GO-PS@PF in Fig. 1C, PF@PS templates are uniformly wrapped by GO sheets after the subsequent filtration due to the electrostatic interaction and hydrogen bond. The restacking of GO sheets in the GO-PF@PS is inhibited due to the intercalation of PF@PS templates, so a crumpled morphology in the range of tens to hundreds of nanometers is observed in the TEM image in Fig. 1D. By contrast, GO shows densely stacked structures (Fig. S2). Such a restacking inhibited characteristic GO sheets is beneficial to the exfoliation of graphene sheets during the calcination process. As shown in Fig. 1E, the HMCS is well intercalated into the graphene sheets throughout the entire sample after the calcination due to the intrinsic flexibility of graphene sheets and the template-directing function of PF@PS, so the aggregation of graphene is effectively prevented. In addition, GO sheets wrapping PF@PS templates are interconnected with each other, which is appropriate to preserve the graphene-based wrapping structure of GHMCS.[31] The TEM image in Fig. 1F further confirms that the HMCS is uniformly coated by graphene sheets in the GHMCS, and the HMCS obtained from the PF@PS is inserted in graphene sheets, which avoids the face-to-face van der Waals contact of neighboring graphene sheets. Moreover, gaseous products are liberated due to pyrolysis of PF@PS templates, and thus numerous micropores and mesopores are formed on the walls of HMCS (Fig. S3).[32] Hence, abundant micro- and mesopores in the HMCS are introduced into the wrappings in individual graphene sheets, and macropores are formed correspondingly due to the removal of PS spheres. The graphene-coated structure is obviously presented in the magnified SEM images in Fig. 1G. The HMCS is tightly coated by graphene sheets, and the individual graphene sheet connects with each other to form an interconnected network. In addition, the graphene wrappings consist of flexible and transparent graphene sheets with a few layers observed from the TEM image (Fig. 1H), providing a conductive network for the whole architectures. Meanwhile, the liberation of gases from the pyrolysis of PS and PF can incorporate into the layered graphene sheets and results in a rapid volume expansion, which accelerates the sufficient exfoliation of graphene and form loosely-stacking graphene architectures. This also contributes to the formation of several open porous channels in the GHMCS after the calcination.[33, 34] In a word, with this hierarchically porous structure and high exfoliation of graphene, the GHMCS would provide numerous channels for salty ions transport for the CDI application.

The structural changes of GO, PS, PF@PS and GO-PS@PF during the calcination process were detected by the TG measurement, and the results are presented in Fig.2A. The TG curve of GO shows two significant weight loss events. The first events in the temperature range of 100-120 ^{o}C is related to the adsorbed water, while the second one in the temperature range of 170-250 ^{o}C is attributed to the decomposition of oxygen-containing functional groups. This indicates that GO is thermally reduced and graphene is finally formed. According to the previous report, the PS starts to lose weight upon heating at about 400 ^{o}C and is totally pyrolyzed at about 600 ^{o}C.[35] The TG curve of PS@PF exhibits two weight loss stages, which are separately in the temperature range of 250–350 ^{o}C and 350–450 ^{o}C. These losses are attributed to water removal from the carbonization of PF and the predominant pyrolysis of PS, respectively. Notably, the TG curve of GO-PF@PS has three weight losses. Specially, the weight loss below 250 ^{o}C is belong to the removal of oxygen-containing functional groups and adsorbed water. The other two obvious weight losses are attributed to the carbonization of PF at about 250 ^{o}C and the pyrolysis of PS at about 350 ^{o}C. It should be noted that the TG curve of GO-PF@PS becomes smooth upon 600 ^{o}C, indicating the deeply thermal reduction of GO, high carbonization of PF, and complete removal of PS. Furthermore, the weight losses of GO-PF@PS are smaller than that of PF@PS and GO upon to 900 ^{o}C, indicating the coexistence of thermally derived graphene and HMCS. Meanwhile, because volatile gaseous species such as CO_2 and H_2O are released during the pyrolysis of PS and PF, the restacking of graphene can be further inhibited and the oxygen-containing groups in deep regions of CHMGS can also be removed correspondingly.[33]

The successful removal of oxygen-containing groups of GHMCS was further confirmed by the XPS measurement. The C1s spectrum of GHMCS is shown in Fig. 2B. It is clear that four

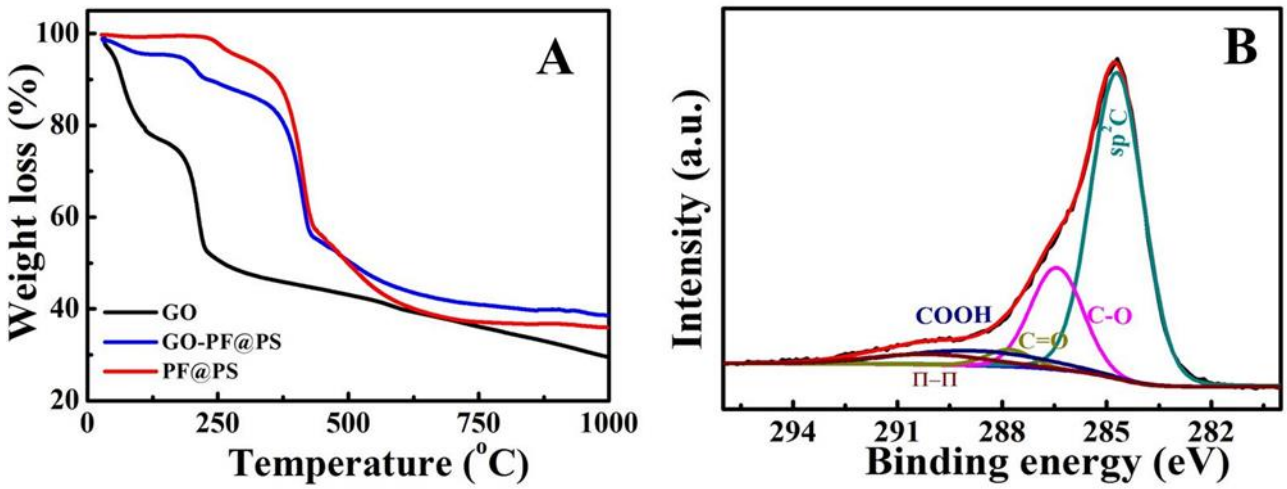

Fig. 2 (A) TG curves of GO,GO-PF@PS and PF@PS; (B) XPS spectrum of GHMCS.

Cite this: DOI: 10.1039/c0xx00000x

www.rsc.org/xxxxxx

ARTICLE TYPE

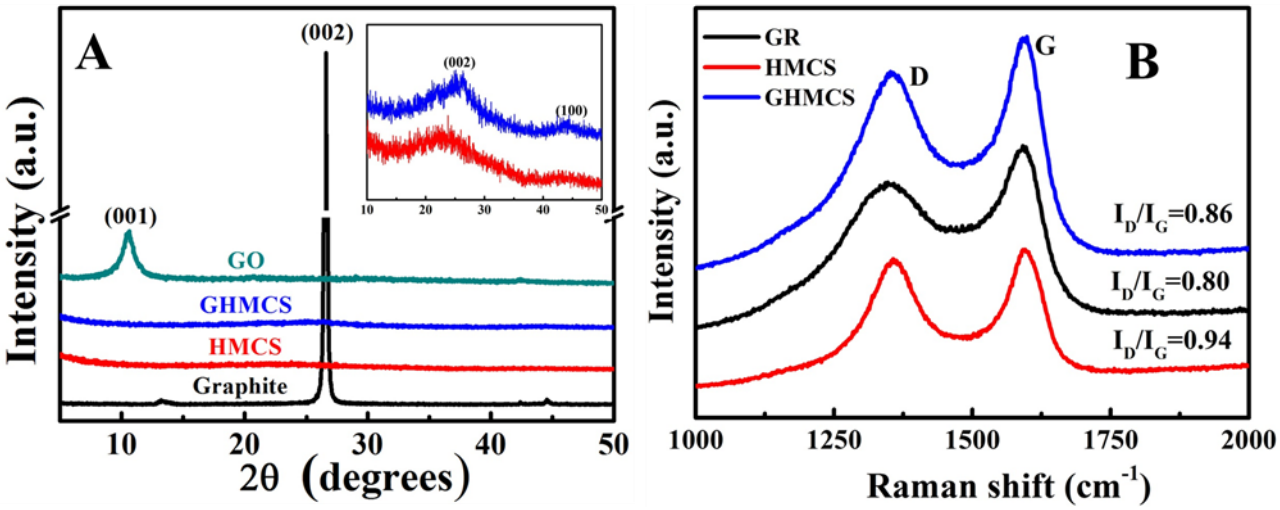

Fig. 3 (A) XRD patterns and (B) Raman spectra of the prepared samples. The inset of (A) is the local enlarged XRD patterns of GHMCS and HMCS.

peaks centered at 284.6, 286.4, 287.8 and 288.8 eV exist in the GHMCS, which are attributed to the sp^2 aromatic rings, C-O, C=O and COOH, respectively.[21] As compared to the XPS spectra of GO (Fig. S3), the intensity of sp^2C in the GHMCS is evidently stronger than that of GO, while all the peaks of oxygen-containing groups are decreased noticeably. These results indicate that the GHMCS has a high reduction degree and the conjugated structure is well recovered simultaneously after the calcination. In addition, the PF obtains a high carbonization degree due to the calcination. Notably, an additional peak at 290.1 eV assigned to the π-π* shake-up signal for the sp^2C appears in the spectra of GHMCS, suggesting the formation of graphene and the final production has a high graphitized degree. In brief, the GHMCS has a deep deoxygenation and graphitized degree due to the sufficiently thermal reduction.

The XRD has been used to determine the crystalline structure of resulting samples. Fig. 3A displays XRD patterns of GHMCS, GO, HMCS and graphite. GO has an intense peak at the 2θ=10.3 ° due to the existence of abundant oxygen-containing groups and thus GO shows a much larger interlayer distance than graphite. In contrast, the strong peak (001) of GO has disappeared and a broad hump at 2θ = 26 ° appears at the XRD pattern of GHMCS, indicating the successful removal of oxygen-containing groups in the GHMCS owing to the high-temperature calcination.[36] The effective exfoliation of graphene sheet can also been confirmed, because the intercalation of HMCS alleviate the aggregation of individual graphene sheets. As compared to the sharp (002) peak of graphite, the (002) peak of GHMCS is quite weaker and broader, further demonstrating that graphene sheets in the GHMCS are only loosely stacked due to the unique structure and the liberation of gases during the high-temperature calcination, which is in good accordance with SEM and TEM images.[37] In contrast, the GR shows a sharper (002) peak than the GHMCS (Fig. S4), which further demonstrates that graphene can hardly be exfoliated to individual sheets with the absence of HMCS. As seen in the inset of Fig. 3A, two broad diffraction peaks at 26 ° and 43 ° relating to the typical (002) and (100) planes of graphitic material respectively can be observed for both the samples.[38] The (002) and (100) peak of GHMCS is a bit stronger than that of HMCS, indicating the GHMCS arising from the combination of HMCS and GR can enhance the graphitization degree to some extent. Hence, the GHMCS has a better conductivity due to graphene wrapping around the HMCS, which is beneficial to the construction of interconnected conductive networks, and thus lower the energy consumption during the CDI process.[10]

Raman spectroscopy is an effect tool to reflect the structural changes of graphene layers on the atomic level. As shown in Fig. 3B, the peak located at 1350 cm^{-1} is the D band related to the edges, defects and structural disorders in solid carbons. The G band arises from the first-order scattering of E_{2g} mode of sp^2 carbon atoms. The intensity ratio of two bands (I_D/I_G) proves the graphitization degree of carbon solids, and a lower value always represents a higher degree of graphitization.[39] The GHMCS shows a decreased I_D/I_G value (I_D/I_G=0.86), as compared to the HMCS (I_D/I_G=0.94), respectively. This indicates an improved graphitized degree of GHMCS, associating with its superior electric conductivity, which agrees with the XRD analysis. Besides, the I_D/I_G value of GR is 0.80, and the increased value of GHMCS indicates that the successful introduction of HMCS between the interlayer of graphene sheets, and thus the disorder of structure increases correspondingly, associated with the TEM and SEM images.[40] Combining the advantages of HMCS and graphene, the GHMCS has a hierarchical pore system and improved conductivity, which has been demonstrated to be beneficial to the ion transport and lower inner resistance in the CDI application.[10] The enhanced conductivity can be further confirmed by the EIS and IR drop in the GC measurement

Cite this: DOI: 10.1039/c0xx00000x

www.rsc.org/xxxxxx

ARTICLE TYPE

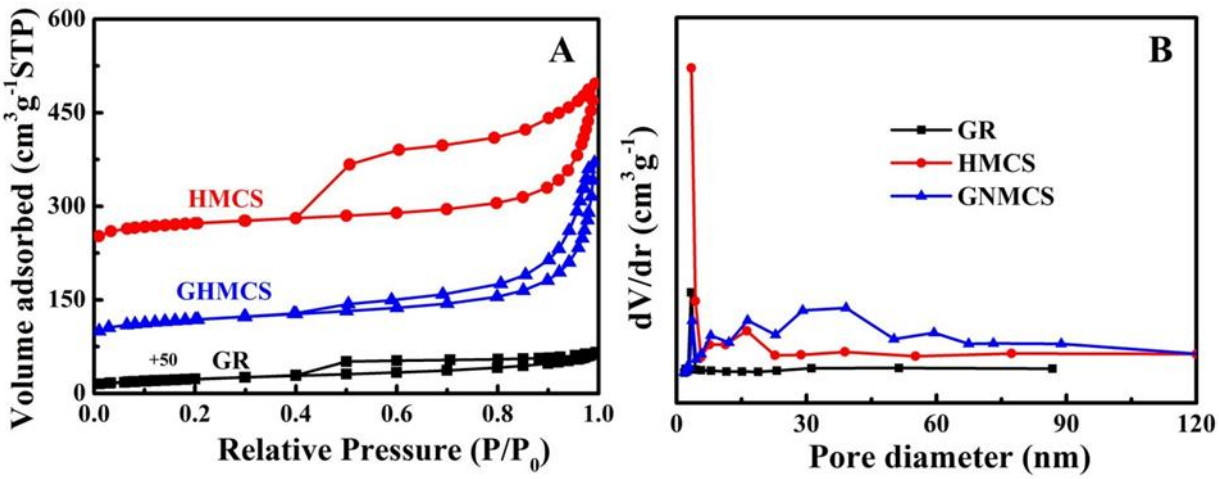

Fig. 4 (A) N_2 sorption isotherms and (B) pore size distribution of the GHMCS, HMCS and GR.

analysis in the following discussion.

The pore structure and specific surface area of GHMCS were tested by the N_2 adsorption-desorption. Fig. 4A shows the N_2 sorption isotherms and the BJH pore size distribution plots of GHMCS, HMCS and GR. The GHMCS has a typical type IV isotherm with a hysteresis loop at a wide pressure range (p/p_0 = 0.4-1.0), indicating the existence of mesopores and macropores.[41] The specific surface area of GHMCS is 400.4 m^2 g^{-1}, which is much higher than that of GR (83.2 m^2 g^{-1}) obtained with the absence of PF@PS templates. The generation of HMCS as "spacer" can impede the aggregation of individual graphene sheets and keep the graphene coated structure due to the spacing and supporting effect of HMCS during the calcination process. The sufficient exfoliation of graphene results in an increased specific surface area of GHMCS, which can provide more adsorption site and accessible area for salty ions and thus could enhance the CDI capacity. In contrast, the HMCS has a bit larger specific surface area of 512.4 m^2 g^{-1}, but the external area is only 109.6 m^2 g^{-1}, which is lower than that of GHMCS (122.5 m^2 g^{-1}) (Table S1). In other words, the increased external area is helpful to the increase the accessible surface area for ion accumulation during the CDI process. The BJH pore size distribution profiles derived from desorption branches of isotherms were shown in Fig. 4B. Clearly, the GHMCS shows a wide pore distribution due to the existence of hierarchical pore system. The numerous mesopores and micropores are most in the wall of HMCS, and macropores are resulted from the hollow cavity. In addition, many open pores are also fabricated due to the release of gaseous production. Therefore, the GHMCS derived from the PF@PS templates is effectively exfoliated and thus has a higher surface area and hierarchically porous structure, which will facilitate more accessible surface area and pathways for the salty ions during the CDI application.

3.2 Electrochemical performance

As a demonstration of the advantage of its unique structure, the electrochemical performances of GHMCS were deeply investigated. The CV curves in Fig. 5A exhibit a nearly rectangular shape with no redox peaks, indicating that the CV behaviors are resulted from the ideal electrical double-layer capacitance (EDLC) at the electrode/solution interface rather than Faradic reactions.[15, 42] Generally speaking, the closed area of CV curve represents the ion adsorption capacity, and a higher area is much expected for an increased specific capacitance. With the same electrode preparation and testing conditions, the CV curve of GHMCS electrode has a larger encircled area than that of GR and HMCS, indicating that graphene-based hierarchically porous structure can enhance the electrosorption performance of GHMCS. The specific capacitance of GHMCS calculated from the CV curve is 43.22 F g^{-1}, and much higher than that of HMCS (32.39 F g^{-1}) and GR (23.33 F g^{-1}). Combing the merits of graphene and HMCS effectively, the composite has an evidently improved specific surface area due to the sufficient exfoliation, associated with more exposed surface sites for ion adsorption. Therefore, more ions can participate in the EDL formation at the interfacial region around the GHMCS electrode, and thus an improved specific capacitance is obtained. As the skeleton of GHMCS composite, graphene can serve as the conductive network, associated with decreased inner resistance of GHMCS electrodes. Although the GHMCS has a relatively lower specific surface area than the HMCS, effective and fast ion diffuse into the interior of bulk material can be well realized during the electrosorption process due to the higher conductivity and external surface area.[15, 43] In addition, the HMCS can bridge the graphene planes, so the electrons can continuously transfer through the whole structure and thus effectively increase the conductivity.[17, 44] Furthermore, the intercalation of HMCS with abundant micro- and mesopores in the interlayer of graphene sheets provide more ion transportation channels and a large accessible area for salty ions penetration and accumulation.[10, 45, 46] The open pores from the loosely stacking graphene sheets can

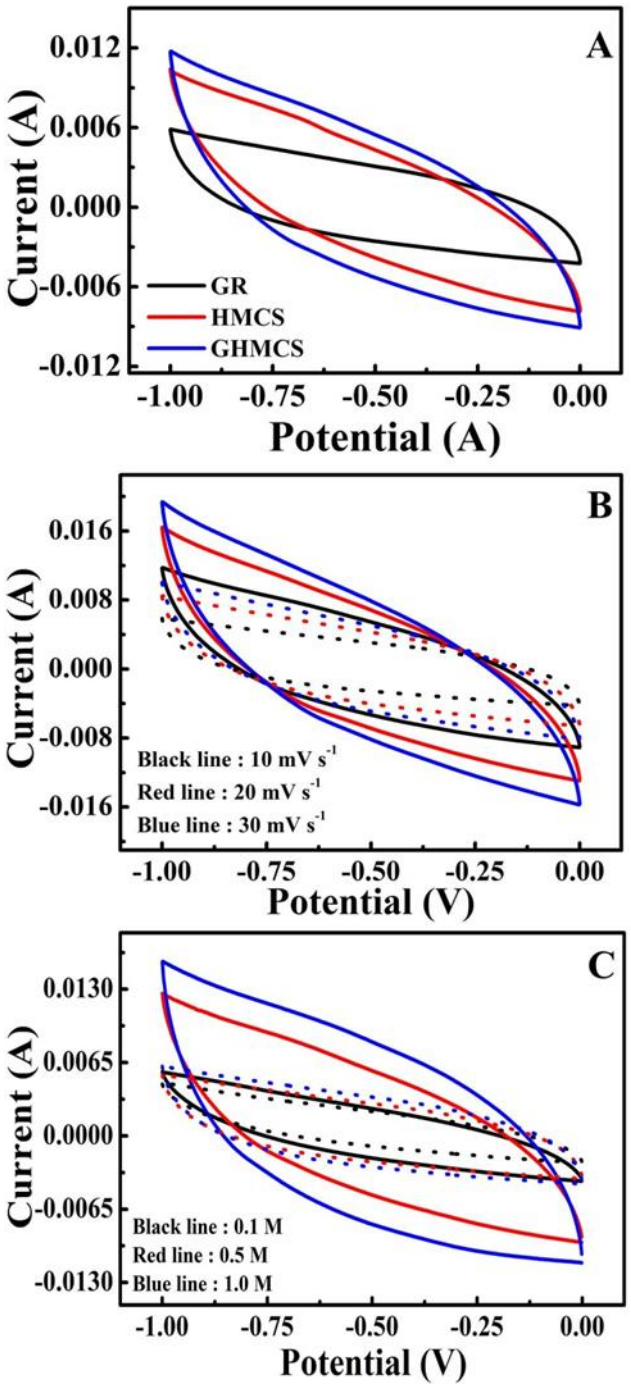

Fig. 5 CV curves of (A) GR, HMCS and GHMCS electrodes at a scan rate of 10 mV s^{-1}; (B) GHMCS and GR electrodes at various scan rates ; (C) GHMCS and GR electrodes at different NaCl concentrations at a scan rate of 10 mV s^{-1} (solid line: GHMCS and dot line: GR). The curves (A and B) were obtained in a 0.5 M NaCl aqueous solution.

also boost the easy accessibility of salty ions into the deep regions of GHMCS electrode.[47] According to the CV analysis, the GHMCS shows an improved electrosorption capacitance, so it could be deduced that a higher deionization efficiency would be obtained.

Fig. 5B shows CV curves of GHMCS at the scanning rates ranging from 10 to 30 mV s^{-1} in a 0.5 M NaCl aqueous solution. Generally speaking, no obvious Faradaic reactions are observed at any scan rate, indicating the EDLC behaviour due to the Coulombic interactions. However, with the increase of scanning rate, the CV curve shows an increased distortion from the typical rectangular and turns to leaf-like shapes. The specific capacitance calculated from the CV curves is 43.22 F g^{-1} for the GHMCS and 23.33 F g^{-1} for GR at 10mV s^{-1}, which is much higher than 21.33 F g^{-1} for the GHMCS and 13.30 F g^{-1} for GR at 30mV s^{-1}. Clearly, a lower scan rate is favourable for a higher specific capacitance. This can be attributed to the following two reasons. Firstly, the salty ions have adequate time to diffuse into the inner pores of electrodes and more salty ions are absorbed on the surface of electrodes, and thus the formation of EDL is complete, associated with a better capacitive behaviour. Oppositely, the salty ions hardly have time to diffuse into the deeper pores of electrode at the high scan rate, which results in a decreased accessible surface area for ion adsorption, and a lower capacitance is shown correspondingly. Besides, the Ohmic resistance of ionic motion in the pores is high at the high scanning rate, which has an obvious influence on the EDL formation behaviour. In addition, the specific capacitance of GHMCS electrode is much larger than GR at any scanning rate, further indicating a better electrosorption performance.

The effect of ion concentration on the electrosorption capacity of GHMCS is also investigated. The CV curves in NaCl aqueous solutions with different concentration (0.1-1.0 M) are shown in Fig. 5C. It is clear that the areas of all CV curves of GHMCS electrode are much larger than that of GR, further demonstrating that the graphene-based hierarchically porous structure favors the electrosorption capacity of GHMCS. Besides, the specific capacitance of electrode is enhanced with the increase of concentration of NaCl aqueous solution, because of the improved accumulation of salty ions on the surface of electrodes at the higher concentration. In addition, a weaker EDL surface overlap effect at the higher concentration also contributes to an improved capacitance.[48] Meanwhile, the conductivity and the maximum energy density of salty solution are enhanced at a higher concentration due to the larger amount of Na^+ and Cl^- ions. However, if the concentration is too high, the CDI efficiency will be influenced due to the coulomb inefficiency caused by the electrode pore volume.[49]

In brief, the GHMCS electrode shows a better capacitive property than the GR one at any concentration and scanning rates. It should be noted that the hierarchically porous structure shortens ion diffusion distance, improves accessible surface area and provides interconnected pathways for ion transportation, so abundant salty ions can be adsorbed on the surface of GHMCS electrode and penetrate into the deeper pores, and thus an enhanced electrosorption ability of GHMCS is shown in the above CV measurements. Furthermore, the GHMCS has relatively higher graphitization degree as revealed by the XRD and Raman analyses. Hence, the GHMCS should be is a desirable candidate for the CDI application due to the above two aspects.

The EIS measurement can be used to detect the electric conductivity of carbon electrode. As shown in Fig. 6, the GHMCS, HMCS and GR electrodes display similar Nyquist plots including a semicircle at the high frequency and a straight spike at the low frequency. According to the previous reports,[17, 50, 51] the intersection of the curves at the real axis in high regions of

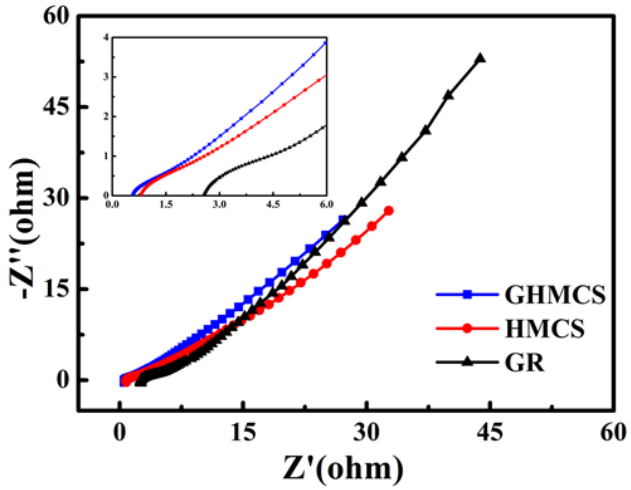

Fig. 6 The EIS presented as Nyquist plots of the GHMCS, HMCS and GR electrodes in a 0.5 M NaCl aqueous solution. The inset is local enlarged frequency region.

frequency represents the equivalent series resistances (ESR), which is resulted from the ionic resistance of saltwater, the intrinsic resistance of electrodes, and the contact resistance at the interface of active material/current collectors. As seen from the inset in Fig. 6, the inner resistance of HMCS is larger than that of GHMCS, demonstrating that graphene wrapping on the surface of discrete HMCS can form conductive network and further enhance the conductivity of GHMCS. In addition, the GHMCS has a higher carbonization degree than the HMCS according to the XRD and Raman analyses, and thus the higher conductivity is obtained. Noteworthy, the ESR of GHMCS electrode is much smaller than that of GR under the same evaluation system, which indicates that effectively exfoliated graphene dramatically decrease the inner resistance of GHMCS.[31] The compact structure of GR leads to a large interface resistance, and modest the conductivity of graphene correspondingly.[52] It should be noted that the smaller ESR means that the GHMCS electrode will show less internal loss and greater charge transport in the CDI process. The diameter of semicircle related to the charge-transfer resistance of the electrodes and the solution interface. As seen from the curves, the radius of GHMCS and HMCS electrodes is small, suggesting the negligible interfacial polarization resistance. The enhanced charge transfer must be associated with the increased contact area between the salty solution and electrode due to the porous structure of GHMCS and HMCS electrodes.[25] As compared to the GHMCS, the GR shows a visible semicircle, because the salty solution can hardly permeate into the compact GR electrode effectively.[53] In the low frequency region, the inclined line is derived from the typical double layered capacitive behaviors due to the surface roughness, the frequency dispersion of electrodes and the low concentration of salty solution.[12, 54] In conclusion, the lower inner resistance consumption of the GHMCS with an improved conductivity benefits a faster charge/discharge rate, which ensures a highly efficient electrosorption behavior.

The discharge curves of all the electrodes obtained from the GC measure are shown in Fig. 7A. It is obvious that the discharge

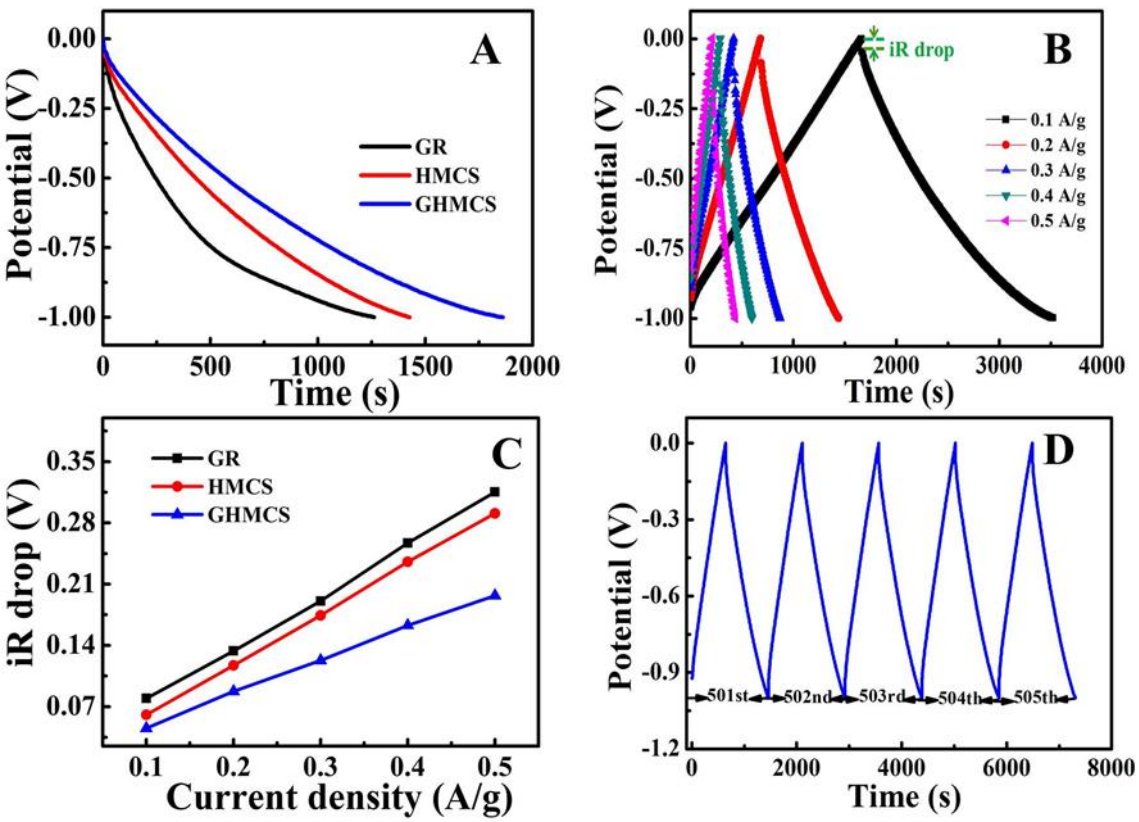

Fig.7 GC curves (A) of GHMCS, HMCS and GR electrodes with a current density of 0.1 A g^{-1}; (B) GHMCS electrode at various current densities; (C) iR drops of the electrodes *vs*. current densities; and (D) continuous GC curves of the GHMCS electrode with a current density of 0.2 A g^{-1}. All the curves were obtained in a 0.5 M NaCl aqueous solution.

Cite this: DOI: 10.1039/c0xx00000x

www.rsc.org/xxxxxx

ARTICLE TYPE

time of GHMCS electrode is visibly longer than that of GR and HMCS, so the GHMCS electrode has a highest specific capacitance.[55] The enhanced capacity may be resulted from the hierarchically porous structure and high conductivity.The macroporous cavity in the GHMCS serving as ion-buffering reservoirs guarantees shorter ion diffusion distances to the interior surfaces of the pores. Meanwhile, mesopores and micropores in the walls of HMCS can provide efficient pathways for the ions penetration and transport. Hence, a large accessible surface area can assure abundant ion adsorbed on the surface of GHMCS electrode. Fig. 7B shows the typical charge-discharge profiles of the GHMCS electrode at a current density window range from 0.1 to 0.5 A g^{-1}. The typical galvanostatic charge-discharge curve of GHMCS electrode displays a typical triangular shape, revealing that the GHMCS electrode exhibits excellent reversibility and an ideal EDLC behaviour due to the deeply thermal reduction and exfoliation, which is in good agreement with the above CV measurements. Obviously, the charge-discharge curve of GHMCS exhibits linear potential-time plots, indicating the rapid I-V response during the whole electrosorption process. As increasing current density, the iR drop can be observed at the beginning of the discharge process, which is correlated with the inherent resistance of salty solution, electronic resistance of electrode and ion diffusion resistance into the inner pore network. The detailed analysis of iR drop change against the current density is shown in Fig. 7C. Evidently, the iR drop of both electrodes is increased with the increasing current densities, which is in accordance with the previous report.[10] The GHMCS electrode has a lower iR drop value than that of HMCS, indicating a reduced inner resistance corresponding with an improved conductivity of the unique graphene-based hierarchical structure.[56] This further confirms that the interconnected conductive network constructed by graphene can enhance the conductivity of GHMCS.[57] In contrast, with the absence of HMCS, the compact structure of GR may lead to a large interface resistance, and thus compromise the conductivity of graphene. In addition, the ESR of electrode can be calculated from the slope of linear correlation between the iR drop and the discharge current density. The slope of GHMCS are significantly smaller than that of GR and HMCS electrodes, further demonstrating the GHMCS has a lower overall resistance associated with a superior conductivity.[58] This is in good accordance with the EIS analysis, and both confirm the combination of HMCS and GR renders the composite electrode a reduced inner resistance, and makes it more suitable for a fast charge/discharge process with a lower resistance during the electrosorption process.

The cycle performance of GHMCS electrode was also investigated by the continuous GC measurement in a current density of 0.2 A g^{-1}. As shown in Fig. 7D, the GC curves of GHMCS electrode well retains a typical triangular shape without any redox peaks after 500 cycles, indicating that the GHMCS electrode keeps a good stability in repeated charge and discharge processes. Besides, no charge-discharge decay is found during the repeated cycle process, demonstrating the GHMCS electrode exhibits an excellent cycling performance. In a word, the GHMCS has a remarkable stability and cyclability, which results from the interconnected conductive network and hierarchically porous structure.

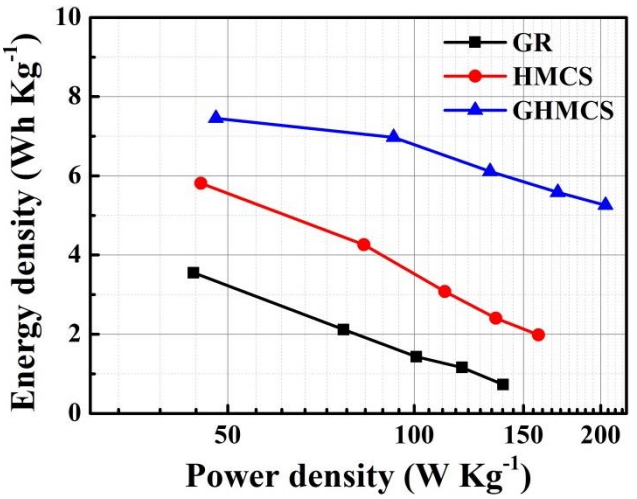

Fig.8 Ragone plots of GHMCS, HMCS and GR symmetric electrodes.

To further investigate the electrochemical performance of GHMCS, the GHMCS//GHMCS, HMCS//HMCS and GR//GR symmetric electrodes were tested galvanostatically between 0 and 1.0 V in a 0.5 M NaCl aqueous solution. The Ragone plots shown in Fig. 8 present the relationship between the power density and energy density at current densities ranging from 0.1 to 0.5 A g^{-1}. Generally speaking, the energy density is decreased with the increase of power density, which is in accordance with the previous reports.[31, 59-61] Obviously, the power delivery of GHMCS electrode is the highest for the same energy density as compared to the GR and HMCS at any current density, which indicates that the GHMCS with highly conductive network and hierarchically porous structure has an enhaced rate performace. Calculated according to previously described methods, [15] the maximum energy density of GHMCS electrodes is 7.46 Wh Kg^{-1} (with a power density of 47.85 W Kg^{-1}.),which is higher than that of HMCS and GR (5.81 and 3.55 Wh Kg^{-1}) at 0.1 A g^{-1}. More importantly, the energy density of GHMCS electrode drops slowly from 7.46 to 5.26 Wh Kg^{-1}. In contrast, the HMCS electrode shows significant energy drops (5.81 to 1.98 Wh Kg^{-1}), which is caused by its ESR due to the lower conductivity. The GR electrode has a low energy density 3.55 Wh Kg^{-1} at 0.1 A g^{-1} and a quick energy drop (3.55 to 0.73 Wh Kg^{-1}) due to its compact structure hindering the ion diffusion. In a word, the synergistic effects of graphene and HMCS contribute to the excellent rate perforamce and low energy consumption of the GHMCS electrode. Hence, the GHMCS is a promising electrode material for the CDI application due to the low energy cost and the high power output.

3.3. CDI behaviors

Taking full advantage of the hierarchically porous structure and excellent conductivity, the deionization behaviors of GHMCS electrode were carried out by batch mode experiments in a NaCl aqueous solution with an initial conductivity of 68.5 μS cm^{-1}. A pair of electrodes separated by an insulating spacer was assmble to a sandwich structure in accordance with our previous reports.[21, 30] The CDI performance under a direct voltage of 1.6 V were investigated and all the charge processes were carried out about 120 min, and the resulted CDI profiles are presented in Fig. 9. Obviously, the conductivity of salty solution decreases sharply at the beginning of CDI process, which indicates that the salty ions can be quickly and easily absorbed by the electrodes. With the time going by, the changes of conductivity become slow until reaching the adsorption equilibrium, because the constancy of electrosorption is hindered by the electrostatic repulsion between the adsorbed ions. More importantly, the declining trend of GHMCS electrodes is noteworthy, while the curve of GR is smooth during the whole CDI process, suggesting the GR is easy to be fully charged under the same CDI experiment conditions. In addition, the GHMCS electrode exhibits a higher deionization rate performance than the GR or HMCS electrode, because much more salty ions are absorbed by the GHMCS electrode at any period of the CDI process. After 120 min, the conductivity of NaCl aqueous solution reduced to 15.8 μS cm^{-1}, and the electrosorption capacity of GHMCS electrode is calculated to be 2.3 mg g^{-1}, larger than that of HMCS (2.0 mg g^{-1}) and more than twice that of GR (1.0 mg g^{-1}). Furthermore, the GHMCS exhibits a larger electrosorption capacity than the porous carbon or graphene in literatures (0.6-2.0 mg g^{-1}).[4, 23, 62, 63] The enhanced electrosorption capacity is attributed to the following reasons. The HMCS incorporated into graphene improves the specific surface area, so more ion adsorption sites are offered during the CDI process, associated with an enhanced desalination performance. The hierarchical pore structure provides numerous accessible ion diffusion channels and shortens ion diffusing distance, and thus favours faster ion transport into the interior of GHMCS electrode. Besides, the interconnected conductive networks decrease the inner resistance of GHMCS, which attributes to less applied voltage consumption of the electrode itself and accelerate salty ion movement during the CDI process. In a word, the GHMCS with a hierarchical pore structure, interconnected conductive networks and large specific surface area is an excellent candidate material for the CDI application.

Conclusions

In conclusion, the GHMCS is rationally designed and originally used as the high performance electrode material for CDI. The GHMCS with hierarchical pore structure and interconnected conductive networks is obtained by a simple template-directing method. The structural features induce synergistic effects of graphene and HMCS, leading to remarkable electrochemical properties and excellent CDI performance. The morphology and structure analyses demonstrate that the HMCS is well intercalated into the interlayer of graphene, which effectively prevent the aggregation and restacking of graphene. Besides, the introduction of abundant micro- and mesopores improves the specific surface area and provides more nanochannels for ion transport and accommodation. In addition, graphene coated on the surface of

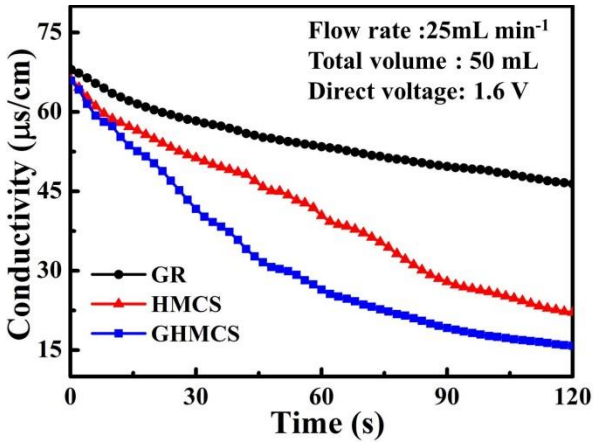

Fig.9 CDI profiles of the GR, HMCS and GHMCS electrodes.

HMCS constructs a conductive network, which enhances the conductivity of GHMCS and ensures the fast charge carrier and transport. The results of electrochemical characterization indicate that the as-prepared GHMCS electrode has higher specific capacitance, lower inner resistance and good stability, which is closely related to structural features of GHMCS. The CDI performance is detected by the batch mode apparatus, which demonstrates that the GHMCS electrode shows an enhanced CDI capacity than that of GR and HMCS. Therefore, the GHMCS is demonstrated to be a suitable and desirable material for energy and electrochemistry.

Acknowledgements

The authors acknowledge the support of the Science and Technology Commission of Shanghai Municipality (13NM1401200), National Natural Science Foundation of China (51108258), and Shanghai Special Foundation for Cultivation of Youth Teacher from Universities (B.37-0407-11-002). The authors would like to thank Mr W. J. Yu from the Analysis and Test Center of SHU for help with the TEM measurements.

Notes and references

Research Center of Nano Science and Technology, School of Materials Science and Engineering, Shanghai University, Shanghai 200444, China. Fax: 86 21 66136079; E-mail: dszhang@shu.edu.cn

† Electronic Supplementary Information (ESI) available: [SEM image of GO, TEM images of PS and HMCS; XPS spectrum of GO; XRD patterns of GHMCS and GR and detailed analysis of surface areas of each sample]. See DOI:10.1039/b000000x/

1. S. J. Kim, S. H. Ko, K. H. Kang and J. Y. Han, *Nat.Nanotehcol*, 2010, **5**, 297-301.
2. S. Porada, R. Zhao, A. van der Wal, V. Presser and P. M. Biesheuvel, *Prog Mater Sci*, 2013, **58**, 1388-1442.
3. Z. Peng, D. S. Zhang, L. Y. Shi, T. T. Yan, S. Yuan, H. R. Li, R. H. Gao and J. H. Fang, *J Phys Chem C*, 2011, **115**, 17068-17076.
4. L. D. Zou, L. X. Li, H. H. Song and G. Morris, *Water Res*, 2008, **42**, 2340-2348.
5. H. J. Yin, S. L. Zhao, J. W. Wan, H. J. Tang, L. Chang, L. C. He, H. J. Zhao, Y. Gao and Z. Y. Tang, *Adv Mater*, 2013, **25**, 6270-6276.
6. C. J. Gabelich, T. D. Tran and I. H. Suffet, *Environ Sci Technol*, 2002, **36**, 3010-3019.
7. S. Porada, L. Borchardt, M. Oschatz, M. Bryjak, J. S. Atchison, K. J. Keesman, S. Kaskel, P. M. Biesheuvel and V. Presser, *Energ Environ Sci*, 2013, **6**, 3700-3712.
8. H. Oda and Y. Nakagawa, *Carbon*, 2003, **41**, 1037-1047.

9. C. Tsouris, R. Mayes, J. Kiggans, K. Sharma, S. Yiacoumi, D. DePaoli and S. Dai, *Environ Sci Technol*, 2011, **45**, 10243-10249.
10. X. R. Wen, D. S. Zhang, L. Y. Shi, T. T. Yan, H. Wang and J. P. Zhang, *J Mater Chem*, 2012, **22**, 23835–23844.
11. Z. S. Wu, Y. Sun, Y. Z. Tan, S. Yang, X. Feng and K. Mullen, *J Am Chem Soc*, 2012, **134**, 19532-19535.
12. N. Brun, S. R. S. Prabaharan, C. Surcin, M. Morcrette, H. Deleuze, M. Birot, O. Babot, M. F. Achard and R. Backov, *J Phys Chem C*, 2012, **116**, 1408-1421.
13. L. L. Zhang and X. S. Zhao, *Chem Soc Rev*, 2009, **38**, 2520-2531.
14. S. L. Zhao, H. J. Yin, L. Du, G. P. Yin, Z. Y. Tang and S. Q. Liu, *J Mater Chem A*, 2013, DOI: 10.1039/C1033TA14809B.
15. Z. Peng, D. S. Zhang, L. Y. Shi and T. T. Yan, *J Mater Chem*, 2012, **22**, 6603-6612.
16. Z. L. Wang, D. Xu, H. G. Wang, Z. Wu and X. B. Zhang, *ACS Nano*, 2013, **7**, 2422–2430.
17. O. S. Kwon, T. Kim, J. S. Lee, S. J. Park, H. W. Park, M. Kang, J. E. Lee, J. Jang and H. Yoon, *Small*, 2013, **9**, 248-254.
18. R. Ruoff, *Nat Nanotechnol*, 2008, **3**, 10-11.
19. L. Chen, B. Wei, X. Zhang and C. Li, *Small*, 2013, **9**, 2331-2340.
20. N. Jha, P. Ramesh, E. Bekyarova, M. E. Itkis and R. C. Haddon, *Adv Energy Mater*, 2012, **2**, 438-444.
21. H. Wang, D. S. Zhang, T. T. Yan, X. R. Wen, L. Y. Shi and J. P. Zhang, *J Mater Chem*, 2012, **22**, 23745-23748.
22. H. Wang, D. S. Zhang, T. T. Yan, X. R. Wen, J. P. Zhang, L. Y. Shi and Q. D. Zhong, *J Mater Chem A*, 2013, **1**, 11778-11789.
23. H. B. Li, L. D. Zou, L. K. Pan and Z. Sun, *Environ Sci Technol*, 2010, **44**, 8692-8697.
24. Z. J. Fan, J. Yan, L. J. Zhi, Q. Zhang, T. Wei, J. Feng, M. L. Zhang, W. Z. Qian and F. Wei, *Adv Mater*, 2010, **22**, 3723-3728.
25. D. Mhamane, A. Suryawanshi, S. M. Unni, C. Rode, S. Kurungot and S. Ogale, *Small*, 2013, **9**, 2801-2809.
26. K. Zhang, L. L. Zhang, X. S. Zhao and J. Wu, *Chem Mater*, 2010, **22**, 1392-1401.
27. L. Deng, G. Zhu, J. Wang, L. Kang, Z.-H. Liu, Z. Yang and Z. Wang, *J Power Sources*, 2011, **196**, 10782-10787.
28. S. Chen, J. Zhu, L. Qiu, D. Li and X. Wang, *Chem. Eur. J.*, 2013, **19**, 7631-7636.
29. J. Zhang, Y. Jin, C. Li, Y. Shen, L. Han, Z. Hu, X. Di and Z. Liu, *Applied Catalysis B: Environmental*, 2009, **91**, 11-20.
30. D. S. Zhang, X. R. Wen, L. Y. Shi, T. T. Yan and J. P. Zhang, *Nanoscale*, 2012, **4**, 5440-5446.
31. B. Gi. Choi, M. H. Yang, W. H. Hong, J. W. Choi and Y. S. Huh, *ACS Nano*, 2012, **5**, 4020–4028.
32. A. H. Lu, T. Sun, W. C. Li, Q. Sun, F. Han, D. H. Liu and Y. Guo, *Angew Chem Int Ed* 2011, **50**, 11765-11768.
33. Z. Q. Niu, J. Chen, H. H. Hng, J. Ma and X. D. Chen, *Adv Mater*, 2012, **24**, 4144-4150.
34. C. M. Chen, Q. Zhang, C. H. Huang, X. C. Zhao, B. S. Zhang, Q. Q. Kong, M. Z. Wang, Y. G. Yang, R. Cai and D. Sheng Su, *Chem Commun*, 2012, **48**, 7149-7151.
35. S. Y. Li, T. Qian, S. S. Wu and J. Shen, *Chem Commun*, 2012, **48**, 7997-7999.
36. Q. L. Du, M. B. Zheng, L. F. Zhang, Y. W. Wang, J. H. Chen, L. P. Xue, W. J. Dai, G. B. Ji and J. M. Cao, *Electrochim Acta*, 2010, **55**, 3897-3903.
37. X. Xia, J. Tu, Y. Mai, R. Chen, X. Wang, C. Gu and X. Zhao, *Chem. Eur. J.*, 2011, **17**, 10898-10905.
38. S. W. Woo, K. Dokko, H. Nakano and K. Kanamura, *J Mater Chem*, 2008, **18**, 1674-1680.
39. X. R. Wen, D. S. Zhang, T. T. Yan, J. P. Zhang and L. Shi, *J Mater Chem A*, 2013, **1**, 12334-12344.
40. D. P. He, K. Cheng, T. Peng, M. Pan and S. C. Mu, *J Mater Chem A*, 2013, **1**, 2126-2132.
41. X. Xin, X. F. Zhou, F. Wang, X.Y.Yao, X. X. Xu, Y. M. Zhu and Z .P. Liu, *J Mater Chem*, 2012, **22**, 7724–7730
42. H. B. Li, L. K. Pan, C. Y. Nie, Y. Liu and Z. Sun, *J Mater Chem*, 2012, **22**, 15556-155561.
43. A. Vu, X. Li, J. Phillips, A. Han, W. H. Smyrl, P. Buhlmann and A. Stein, *Chem Mater*, 2013, **25**, 4137–4148.
44. T. Xie, W. Lv, W. Wei, Z. Li, B. Li, F. Kang and Q. H. Yang, *Chem Commun*, 2013, **49**, 10427-10429.
45. C. X. Guo and C. M. Li, *Energ Environ Sci*, 2011, **4**, 4504-4507.
46. K. Tang, L. Fu, R. J. White, L. Yu, M.-M. Titirici, M. Antonietti and J. Maier, *Adv Energy Mater*, 2012, **2**, 873-877.
47. G. H. Moon, Y. Shin, D. Choi, B. W. Arey, G. J. Exarhos, C. Wang, W. Choi and J. Liu, *Nanoscale*, 2013, **5**, 6291-6296.
48. T. Y. Ying, K. L. Yang, S. Yiacoumi, C. Tsouris and E. S. Vittoratos, *Langmuir*, 2011, **17**, 1961-1969.
49. M. Andelman, *Sep Purif Technol*, 2011, **80**, 262-269.
50. J. W. Lang, X. B. Yan, W. W. Liu, R. T. Wang and Q. J. Xue, *J Power Sources*, 2012, **204**, 220-229.
51. Y. M. He, W. J. Chen, X. D. Li, Z. X. Zhang, J. C. Fu, C. H. Zhao and E. Q. Xie, *ACS Nano*, 2013, **7**, 174–182.
52. B. G. Choi, S. J. Chang, Y. B. Lee, J. S. Bae, H. J. Kim and Y. S. Huh, *Nanoscale*, 2012, **4**, 5924-5930.
53. J. H. Lee, N. Park, B. G. Kim, D. S. Jung, J. H. K. Im and J. W. Choi, *ACS Nano*, 2013, **1**, 9366–9374.
54. J. Gamby, P. L. Taberna, P. Simon and J. F. F. M. Chesneau, *J Power Sources*, 2001, **101**, 109-116.
55. D. S. Zhang, T. T. Yan, L. Y. Shi, Z. Peng, X. R. W. and and J. P. Zhang, *J Mater Chem*, 2012, **22**, 14696–14704.
56. H. B. Wang, Z. H. Liu, X. Chen, P. X. Han, S. M. Dong and G. L. Cui, *J Solid State Electr*, 2010, **15**, 1179-1184.
57. J. Zhu, D. Yang, X. Rui, D. Sim, H. Yu, H. E. Hoster, P. M. Ajayan and Q. Yan, *Small*, 2013, **9**, 3390-3397.
58. Z. Lei, N. Christov and X. S. Zhao, *Energ Environ Sci*, 2011, **4**, 1866-1873.
59. L. L. Zhang, X. Zhao, M. D. Stoller, Y. Zhu, H. Ji, S. Murali, Y. Wu, S. Perales, B. Clevenger and R. S. Ruoff, *Nano Lett*, 2012, **12**, 1806-1812.
60. H. Gao, F. Xiao, C. B. Ching and H. Duan, *Acs Appl Mater Inter*, 2012, **4**, 2801-2810.
61. Z. B. Lei, N. Christov and X. S. Zhao, *Energ Environ Sci*, 2011, **4**, 1866-1873.
62. Z. Peng, D. S. Zhang, T. T. Yan, J. P. Z. and and L. Y. Shi, *Appl Surf Sci*, 2013, **282**, 965-973.
63. L. X. Li, L. D. Zou, H. H. Song and G. Morris, *Carbon*, 2009, **47**, 775-781.